Journal of Applied Fluid Mechanics, Vol. 18, No. 11, pp. 2837-2851, 2025.
Available online at www.jafmonline.net, ISSN 1735-3572, EISSN 1735-3645.
https://doi.org/10.47176/jafm.18.11.3364

Performance Enhancement of Shock Wave Assisted Drug Delivery Based on Converging Shock Tube Design

Z. Ansari[1], K. Das[1†] and R. B. Pallekonda[2]

[1] *Department of Mechanical Engineering, National Institute of Technology Saitsohpen, Sohra-793108, Meghalaya, India*
[2] *Department of Mechanical Engineering, National Institute of Technology Warangal, Telangana- 506004, India*

†*Corresponding Author Email: koushik.das@nitm.ac.in*

ABSTRACT

The development of needleless drug delivery systems (NDDS) has garnered a promising alternative to traditional needle-based methods. This work emphasizes an effort to utilize shock waves for NDDS. The NDDS consists of a shock tube and a delivery nozzle separated by a solid hyper-elastic membrane (HEM). For this purpose, consideration is given to a converging shock tube (CST) to analyze the shock dynamics and enhance the pressure intensity near the HEM. The fluid-structure interaction enables the energy transfer from the shock wave to the membrane, resulting in elastic deformation and propelling liquid medicines through the delivery nozzle. ANSYS Fluent 2023 is employed to model the 2-D axisymmetric domain of NDDS to investigate the impact of different parameters and factors on converging channel geometry. The numerical model is validated using empirical relations and previously published experimental data. In addition, COMSOL Multiphysics is used to examine the dynamic response of the membrane and capture drug ejection velocity. The analysis culminated in the development of a novel ST geometry featuring a converging design with flat segment for better performance. The study resulted in the use of a 60 mm converging channel with 4.76o inclination followed by a 30 mm flat segment. The modification shows almost 2.5 times enhancement in reflected pressure compared to the plane shock tube and approx. 1.3 times compared to CST. Furthermore, it is revealed that the shock strength (P2/P1) and reflected shock pressure (P5) significantly affect the ejection velocity. Ultimately, the system achieved an enhanced reflected pressure and improved drug ejection velocity of 99 m/s.

Article History

Received January 13, 2025
Revised April 1, 2025
Accepted June 17, 2025
Available online September 3, 2025

Keywords:

Shock wave
Converging shock tube
Reflected pressure intensity
Fluid-structure interaction
Jet velocity

1. INTRODUCTION

Shock waves are a dynamic phenomenon with several applications in various fields. Shock wave research and control continue to drive advancement and development in a variety of sectors, including aeronautical engineering, metal fabrication industries, and medicine. In the modern period, a shock tube (ST) is a laboratory equipment used to explore flow dynamics and shock wave behaviour. The ST provide a regulated experimental and numerical environment for studying shock wave phenomena. An early study of the compressible fluid flow phenomenon employing ST was published in 1899 (Henshall, 1957). Since then, several projects have been undertaken to further its development. Over the last century, ST research has grown exponentially.

Several researches on the generation of shock waves by ST have been published in order to investigate its potential uses across various fields. Zhang and Kim (2015) and Zhang et al. (2015) performed numerical investigations to simulate the propagation of shock waves and contact surfaces in micro-ST. The investigation explored the impact of ST width on the transmission, attenuation, and boundary layer development of the shock waves. Another study performed by Kjellander et al. (2010) revealed the effect of real gases on shock dynamics. The ionization phenomenon of the gas behind the spherical shock at Mach number 8 has been found to be prominent. Moreover, many studies reported the simulation of flows of solid particles, gas-particle interaction, boundary layer effects, effects of slip wall, no-slip wall conditions, and different species transport effects in the micro-ST (Rasel & Kim 2013; Zhang et al., 2016; Singh et al., 2020). Additionally, the numerical study

Nomenclature

a	sound speed		
a_1	sound speed in driver region	$\vec{V}$	total velocity vector
a_4	sound speed in the driven region	V_s	velocity of shock wave
d	inner diameter of the shock tube	V_{jet}	jet velocity
e	specific internal energy	W	strain energy density function
E	total energy	Y_i	mass fraction of each species
F	deformation gradient tensor	***Greek symbols***	
L	total length of the NDDS	α	inclination angle of the nozzle
L_1	driven section length	γ	specific heat ratio
L_4	driver section length	γ_1	specific heat ratio of driven region gas
L_c	converging channel length from the end wall of ST	γ_4	specific heat ratio of driver region gas
L_d	length of DNC	ε	strain tensor
L_f	length of flat segment	θ	inclination angle of the converging channel
L_s	total length of the shock tube	μ_l	dynamic viscosity of the liquid
M_s	shock Mach number	ρ	density of gases
P	pressure	ρ_m	density of HEM
P_1	initial driven pressure	ρ_l	density of water
P_2	primary shock pressure	***Abbreviations***	
P_4	initial driving pressure	AUSM	Advection Upstream Splitting Methods
P_5	reflected shock pressure	CV	Control Volume
R	gas constant	CST	Converging Shock Tube
r_c	radius of end wall	CSTF	Converging Shock Tube with a Flat Segment
r_d	nozzle diameter	DNC	Delivery Nozzle Chamber
S	stress tensor	FSI	Fluid-Structure Interaction
t	time	HEM	Hyper-Elastic Membrane
T	temperature	NDDS	Needle-less Drug Delivery System
T_1	initial driven temperature	PST	Plane Shock Tube
T_4	initial driver *t*emperature	ST	Shock Tube
u_m	displacement vector		

performed by Mukhambetiyar et al. (2017) on micro ST evaluates the dynamic flow behaviour and propagation of shock on varying diaphragm pressure ratios and various wall boundary conditions. Boulahia et al. (2014) investigated the viscous and reactive hypersonic shock wave flows numerically. Furthermore, Lewin and Skews (2020) have been reported about the shock wave propagation through a varying curved surface. The study revealed the formation of different compound shock waves.

Moreover, Muritala et al. (2015) investigated the intricate flow characteristics that emerge when a shock wave diffracts over a convex curved surface. Bayazidi et al. (2023) optimized a nozzle-diffuser piezoelectric micropump with multiple vibrating membranes using CFD simulations and the Design of Experiment (DOE) method. Their approach improved the pump's efficiency, boosting the flow rate by 34.5% (up to 95.82 mL/min) and minimizing flow reversibility to just 0.05%, making it ideal for precise microfluidic applications like drug delivery. The study reported by Wang & Kong (2023) on the method of reconstruction of shock pressure for military and engineering testing purposes. This study delineated the correlation between surface-reflected and free-field shock wave pressures, accounting for the influence of altitude on shock wave pressure. Additionally, the recent work performed by Yu et al. (2025) investigated that the shape of explosives significantly influenced the shock wave propagation. It was found that with cylindrical charges produced more directional shock waves and spherical charges generated more uniform pressure distributions. In addition, Ali & Mondal (2025) explored the interaction of planar oblique shock waves with a slender body. The results highlighted the extreme sensitivity of the missile's aerodynamics to the location of the shock wave and incidence angle, which could have implications for missile stability and control.

The shock waves have also been used in several biomedical applications, particularly in the field of medicine. A recent advancement in biomedicine is the targeted drug delivery to specific depths within the human body. Houser et al. (2003) and Kazi et al. (2018) reported that traditional needle injections are widely utilized for immunization, which is a primary contributor to the transmission of HIV and other blood-borne viral infections. Needle-less drug delivery systems (NDDS) have emerged as a novel approach for administering drugs to patients, eliminating the requirement of conventional needles for skin puncture (Houser et al., 2003; Kazi et al., 2018). In recent times, there has been a growing interest in NDDS as a significant technological advancement for administering liquid and solid forms of drugs and vaccinations. According to Kendall (2002) and Nakayama et al. (2016), the level of control over penetration depth offered by the instrument surpasses that of traditional hypodermic needles. This process has effectively delivered drugs for many medical conditions, including diabetes, skin diseases, allergies, and asthma. The

numerical study performed by Debnath et al. (2019) on the two-fluid model of blood flow about the spread of a reactive solute in a pulsating flow.

In addition, Liu and Kendall (2007) reported particle injection devices powered by jet propulsion to accelerate micro-particles for transdermal medication delivery. It was observed that the particles were expelled with an average velocity of 200-800 m/s. Menezes et al. (2009) presented a needle-free device to deliver liquids to soft targets. The micro-jet penetrated 1 mm into a 5% gelatine block at an average speed of 200 m/s. Jagadeesh et al. (2011) and Rakesh et al. (2012) developed an NDDS based on controlled detonation to administer liquid medications. Moreover, Rathod and Mahapatra (2017) optimized a shock tube-assisted drug delivery system. They predicted a maximum diaphragm velocity of 335 m/s, which can penetrate 0.126 mm in human skin samples. The experimental study is carried out by Kiyama et al. (2019) to observe the penetration of a focussed liquid jet, moving at approximately 200 m/s, through a gel and animal skin. Furthermore, Portaro et al. (2019) developed a device for delivering high volumes of high-viscosity medications to precise target locations in skin samples. Schramm and Mitragotri (2002) investigated transdermal medication delivery with a jet injector experimentally. The jet velocity was varying between 80 and 100 m/s for a jet diameter of 152 µm. Additionally, Park et al. (2006) designed a biodegradable polymer microneedle aimed at enabling the self-administration of medications and regulated drugs release into the dermis. Their study indicated that these microneedles effectively delivered encapsulated agents beneath the dermis of human bodies and could transport medicines at concentrations of up to 10% by mass.

Recent studies have identified many parameters affecting the efficacy of NDDS. Rane and Marston (2020, 2021) explored the ideal taper angle and orifice configuration to improve the transient behaviour of fluid flow and injection efficacy. In addition, Wang et al. (2021) examined the diffusion mechanisms of drugs in subcutaneous tissue. The study assessed the impact of various nozzle geometries for needle-free jet injectors. Trimzi and Ham (2021) highlighted that needle-free devices provide accurate, regulated, and consistent administration of biopharmaceuticals at varying tissue depths. In addition, Hankare et al. (2022) demonstrated that targeting high-strength viscoelastic materials can enhance penetration and improve fluid delivery. Wang et al. (2022) observed that the diameter and length of the injector nozzle significantly influence jet velocity, penetration depth, and overall injection efficiency.

The main aim of the present work is to enhance the reflected pressure intensity to capture the desired jet velocity (V_{jet}) for NDDS. For this purpose, effort has been made to improve the reflected shock pressure and the overall performance of the system by incorporating a converging channel in the ST. The effects of various characteristics and parameters on the shape of the converging channel are analyzed, and a novel geometric model with a converging shape is developed. The proposed converging shock tube (CST) has not been used before for biomedical purposes. Furthermore, a drug delivery nozzle chamber (DNC) is attached to the CST to capture the V_{jet}. In this regard, numerical simulations on CST are performed using ANSYS Fluent to observe the flow behaviour of shock, as well as pre and post-shock pressure distributions inside the modified ST. Additionally, COMSOL Multiphysics is used to perform the fluid-structure interaction (FSI) simulation on the DNC. Analytical approach and previously published experimental work are utilized to validate the model, solver and methodology.

2. METHODOLOGY AND FORMULATIONS

The 3-D schematic representation of the shock wave-assisted NDDS is depicted in Fig. 1. It consists of an ST and a DNC with a small micronozzle. The ST is divided into high-pressure (driver) and low-pressure (driven) sections by a thin diaphragm, whereas the DNC is separated by a thin hyper-elastic membrane (HEM) from the ST. The immediate rupture of the thin diaphragm generates a strong incident shock wave in the driven area. This incident shock wave travels downstream and reflects after hitting the HEM. Furthermore, the HEM undergoes an elastic deformation without rupture, and the drug is ejected in the form of a microjet at velocity V_{jet}.

The V_{jet} mainly depends on the reflected pressure of the shock wave generated inside the ST (Battula et al., 2016). A higher V_{jet} helps in controlling the targeted drug delivery precisely with minimum drug wastage. Therefore, proper control of the reflected pressure is essential in such devices. For simplicity in the investigations, initially, numerical simulation on the ST is performed by considering various geometrical parameters. Further, the simulation is conducted on DNC to visualize the flow velocity of the jet.

2.1 Geometry

The geometry of the NDDS consists of a plane shock tube (PST) of length L_s with an inner diameter of d and a DNC of length L_d, whereas the total length of the NDDS is L. The high-pressure driver (L_4) and the low-pressure driven sections (L_1) of the tube are separated using a thin diaphragm. For drug delivery work, the ST is connected to a DNC, which is separated by a thin HEM of thickness t_m.

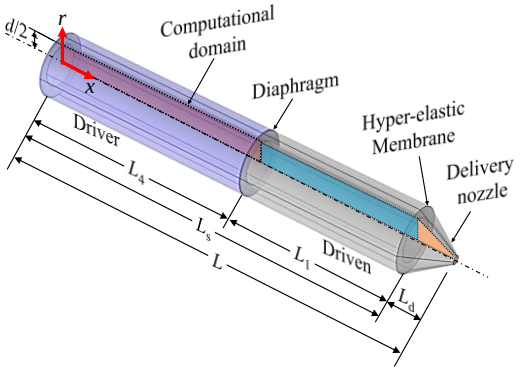

Fig. 1 Pictorial representation of NDDS

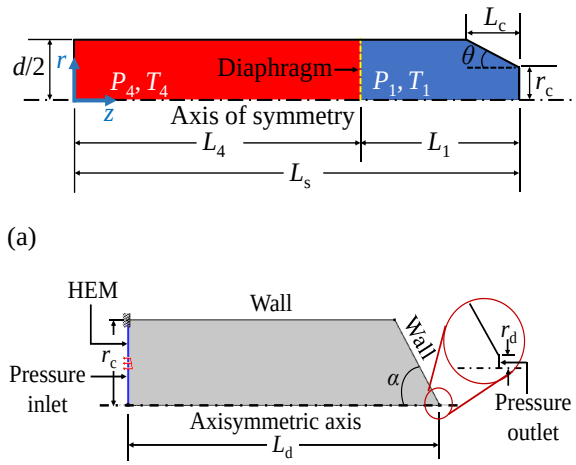

Fig. 2 Computational domain of (a) CST and (b) DNC with boundary conditions

A 2-D axisymmetric domain is considered for the numerical simulation. It reduces the computational cost and time needed to find the solution. For the present numerical study, the PST is modified by designing a converging channel in the driven region called a converging shock tube (CST), as depicted in Fig. 2a. The modifications are made for the enhancement of reflected pressure intensity and overall performance of the system. The optimal shape of the ST is proposed to explore the potential of utilizing the converging channel. The length of the converging channel from the end wall of the ST is considered as L_c inclined at angle θ, whereas the inner radius of the tube is reduced to r_c.

In addition, consideration is given for the DNC to a 20 mm (L_d) in length with nozzle angle $\alpha = 60^o$ and 0.0625 mm of delivery nozzle radius (r_d), whereas the thickness (t_m) of the HEM is 0.2 mm for the present simulation (Fig. 2b). The L_d, α, and r_d are the same as reported by Battula et al. (2016). During the process, the shock wave hits the solid HEM, which further interacts with the liquid of DNC. It leads to the transfer of the intensity from HEM to liquid through FSI. Therefore, elastic deformation of the HEM executes the ejection of liquid microjet from the nozzle. COMSOL Multiphysics well analyzed the FSI simulation and microjet flow on DNC.

2.2 Governing Equations and Boundary Conditions

The shock wave travels at an incredibly high velocity from the driver to the driven section. The flow behaviour of such phenomena is analyzed well by assuming the flow as inviscid (Amir et al., 2008; Kanwar et al., 2015; Zhang et al., 2015). Therefore, the Euler equation derived from the Navier-Stokes equation is applied to the inviscid flow. For a transient, compressible, and inviscid flow coupled with the species-transport equations are as follows

Continuity equation

$$\frac{\partial \rho}{\partial t} + \nabla \cdot \left(\rho \vec{V} \right) = 0 \tag{1}$$

Momentum equations

$$\frac{\partial \left(\rho \vec{V} \right)}{\partial t} + \nabla \cdot \left(\rho \vec{V} \vec{V} \right) = -\nabla P \tag{2}$$

Energy equation

$$\frac{\partial E}{\partial t} + \nabla \cdot \left[\left(E + P \right) \vec{V} \right] = 0 \tag{3}$$

where E depicts the total energy per unit volume, and it includes internal energy (ρe) and kinetic energy $\left(\frac{1}{2} \rho V^2 \right)$. i.e. $E = \rho \left(e + \frac{1}{2} V^2 \right)$. The e denotes the specific internal energy and is equal to $P/(\gamma - 1)\rho$ for an ideal gas (Shankar et al., 2011). Additionally, the working fluids inside the ST are assumed to follow the ideal gas law (Eq. 4)

$$P = \rho R T \tag{4}$$

Species transport equation

The species transport equation is necessary to assess the impacts of different driver and driven gases inside the ST. Since, the flow is governed by Euler equations, so molecular diffusion is neglected. The mixing of species occurs only due to advection, and it moves together with the flow. Considering both the gases in the driver and driven region as ideal gases, the coupled species transport equation is as follows.

$$\frac{\partial}{\partial t} \left(\rho Y_i \right) + \nabla \cdot \left(\rho \vec{V} Y_i \right) = 0 \tag{5}$$

where Y_i denotes the mass fraction of each species

Furthermore, the shock wave exerts a transient pressure on the solid membrane (HEM). The behaviour of a solid membrane is characterized as a hyper-elastic material, which allows large deformations and exhibits nonlinear elasticity. This solid membrane is deformed and interacts with liquid fluid inside the DNC. Therefore, FSI plays a role in coupling the solid (membrane) and fluid interactions. Additionally, for visualizing the flow inside the DNC and to capture the V_{jet}, water is considered as fluid in the DNC. Since, the bulk modulus of water is very high (2.2 x 10^9 Pa), which indicates that substantial pressure variations in the present setup produce negligible changes in density. So, the flow is considered as laminar and incompressible. Therefore, the governing equations of incompressible flow is solved instead of equation of state. The incompressible assumption also reduces the complexity of equation and computational cost of the solver. Hence, structural deformation (elasticity equations) and the governing equations of fluid flow (incompressible Navier-Stokes equations) are solved simultaneously to correctly couple the governing physics and capture the interaction effects accurately. The governing equation for elasticity follows the Cauchy momentum equation and is given as

Stress-Strain (Elasticity) Equation

$$\rho_m \frac{\partial^2 u_m}{\partial t^2} = \nabla \cdot \left(FS \right) \tag{6}$$

where ρ_m is the density of the solid HEM, u_m is the displacement vector of the solid HEM, F denotes the

deformation gradient tensor, and S depicts the second Piola-Kirchhoff stress tensor. The behaviour of the stress-strain relation is nonlinear for HEM (Kim et al., 2012; Wijaya et al., 2019). Therefore, the second Piola-Kirchhoff stress tensor is derived from the strain energy density function and is denoted as

$$S = \frac{\partial W}{\partial \varepsilon} \tag{7}$$

where W depicts the strain energy density function and ε represents the Green-Lagrange strain tensor. Furthermore, the deformation gradient tensor is computed by using the given relation.

$$F = \frac{\partial x}{\partial X} \tag{8}$$

where x depicts the deformed position of a point of the membrane, and X presents the original position (undeformed) of the same point of the membrane. In the present scenario, the Mooney-Rivlin model of two parameters is considered for HEM. Therefore, the strain energy density function for an incompressible Mooney-Rivlin material is as follows.

$$W = C_1\left(I_1 - 3\right) + C_2\left(I_2 - 3\right) \tag{9}$$

where C_1 and C_2 are the material constants, and I_1 and I_2 depict the invariants of the Cauchy-Green deformation tensor. The solver automatically computes I_1 and I_2 from the deformation gradient tensor available in the built-in database library.

Since incompressible fluids exhibit negligible density fluctuations in response to pressure changes, and the variations in pressure also do not cause a substantial change in the internal energy of liquid water. Therefore, the energy equation is excluded from the simulation. The incompressible Navier-Stokes equations for fluid flow inside the DNC are

Continuity

$$\nabla \cdot \vec{V} = 0 \tag{10}$$

Momentum

$$\rho_l\left(\frac{\partial \vec{V}}{\partial t} + \left(\vec{V}\cdot\nabla\right)\vec{V}\right) = -\nabla P + \mu_l \nabla^2 \vec{V} \tag{11}$$

where $\vec{V}$ depicts the fluid velocity vector, ρ_l shows the liquid density, P is the pressure, and μ_l represents the dynamic viscosity of the liquid, which is taken care of by the in-built database library of the solver.

Solving the governing equations (Eq. 1-11) necessitates the specification of process parameters at the boundaries. The boundary conditions associated with the numerical simulation of CST to solve Eq. (1-5) are shown in Fig. 2a. The base of the domain is considered as an axis to solve the axisymmetric solution. The left, right, and top boundaries are considered slip-wall and adiabatic. Nitrogen is used for the driver region gas, and the air is selected for the driven sections to analyze the behaviour of the shock wave in the ST. The pressure in the driver section was set to 25 bar, while the pressure in the driven section was 1 bar. A constant temperature of 298 K for both driver and driven sections has been maintained. The wall boundary condition is immediately transformed into an interior region upon initialization. This procedure was deemed an immediate burst of the diaphragm.

Additionally, the boundary conditions assumed for the DNC domain for solving Eq. (6-11) are depicted in Fig. 2b. The bottom edge of the fluid domain is considered a symmetry axis. The top and left boundary of the fluid domain are considered as no-slip walls, whereas the right edge is considered as pressure outlets. The boundary conditions for HEM are defined as the top node being fixed and the bottom is axial symmetry. The temporal pressure profile obtained from the shock tube simulation is applied on the HEM surface. The adopted numerical procedure to solve the governing equations is discussed next.

2.3 Numerical Simulation Strategy

Numerical simulation is crucial for accurately visualizing and comprehending the internal flow dynamics of the ST. Consequently, the ANSYS Fluent solver is used to solve the governing equations of continuity, momentum, and energy (Eq. 1-5). This involves employing the finite volume method for transient analysis of the ST behaviour. The ST is modelled as an axisymmetric body, chosen for its ability to depict the fluid flow configuration accurately. The analysis of the ST flow field is conducted using the four-stage Runge-Kutta methods based on a density-based implicit solver (Nanda et al., 2017). Additionally, to assess the effects of various driver and driven gases, the species transport equation is also computed. To determine the convective fluxes in the numerical simulations, the flux vector splitting method, known as the Advection Upstream Splitting Method (AUSM), is applied (Nanda et al., 2017). Spatial discretization is described by using a second-order upwind scheme and a green-gauss node-based gradient. The driver and driven sections are patched with corresponding initial pressures, temperatures, and species. The diaphragm is expected to rupture instantly at time zero (Nanda et al., 2017).

Additionally, FSI involves the transfer of energy from the fluid (shock wave) to the solid structure (HEM), causing it to deform and accelerate the liquid microjet. In addition, the solid membrane (HEM) again interacted with the fluid of DNC. Therefore, COMSOL Multiphysics is used to conduct the numerical study on the DNC to capture the flow velocity of the drug. The finite element method (FEM) has been utilized for solving the governing equations (Eq. 6–11) and their associated boundary conditions. The procedure involved a fully coupled transient solver to compute the Eq. (6-9) and Eq. (10-11) simultaneously. The linear solver PARDISO (Parallel Direct Sparse Solver Interface) is employed to solve Eq. (6-11). It provides excellent speed and scalability for addressing intricate issues. A nonlinear solution is started with a tolerance factor of 0.3 and a damping factor of 0.5 to segregate the components of pressure, velocity, displacement, and spatial mesh displacement. All

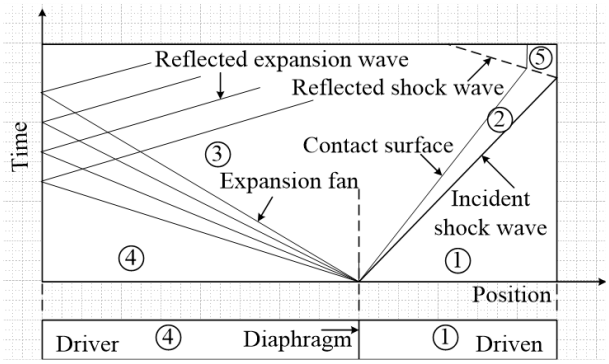

Fig. 3 Graphical representation of shock wave flow inside an ST

investigations employ a termination criterion with a maximum permissible residual of 10^{-10}. This method facilitates reliable convergence for problems exhibiting non-linearities.

2.4 Shock Tube Theory

A shock wave is characterized by an extremely thin region within the flow with a rapid and abrupt change in state. It can typically be simplified as a discontinuity surface propagating into the fluid. Across this surface, all fluid properties, including pressure, velocity, and density, exhibit abrupt discontinuities. The flow across a shock wave adheres to mass, momentum, and energy conservation principles. The results for a normal shock wave in a perfect gas can be derived by applying these conditions. These relations are referred to as Rankine-Hugoniot relations, often known as the ideal shock tube theory. Using these relations, the primary and reflected shock pressures are computed (Fig. 3).

$$\frac{P_2}{P_1} = \frac{2\gamma_1 M_s^2 - (\gamma_1 - 1)}{(\gamma_1 + 1)} \tag{12}$$

$$\frac{P_5}{P_1} = \left[\frac{P_2}{P_1}\right]\left[\frac{(3\gamma_1 - 1)M_s^2 - 2(\gamma_1 - 1)}{(\gamma_1 - 1)M_s^2 + 2}\right] \tag{13}$$

The Mach number is obtained according to the driver (P_4) and driven pressure (P_1)

$$\frac{P_4}{P_1} = \left[1 + \frac{2\gamma_1(M_s^2 - 1)}{(\gamma_1 + 1)}\right]\left[1 - \frac{(\gamma_4 - 1)}{(\gamma_4 + 1)}\left(\frac{a_1}{a_4}\right)\left(\frac{M_s^2 - 1}{M_s}\right)\right]^{-2\gamma_4/\gamma_4 - 1} \tag{14}$$

The sound speed for the respective region can be calculated as follows.

$$V_s = a_1\sqrt{\frac{\gamma_1 + 1}{2\gamma}\left(\frac{P_2}{P_1} - 1\right) + 1} \tag{15}$$

$$a_1 = \sqrt{\gamma RT} \tag{16}$$

where P_1: initial driven pressure, P_2: primary shock pressure, P_4: initial driving pressure, P_5: reflected shock pressure, γ_1, γ_4: specific heat ratio of the respective region, V_s: shock velocity, M_s: shock Mach no., a_1, a_4: sound speeds in respective regions, γ: specific heat ratio, R: gas constant, T: room temperature.

Table 1 Effect of mesh size and error analysis

Grid	G1	G2	G3	G4
Grid size (mm)	1	0.5	0.1	0.05
No. of CVs	3760	15200	368874	1460200
V_s (m/s)	678.53	662.48	657.37	658.21
Error in V_s (%)	-	2.42	0.77	0.12
M_s	1.96	1.91	1.89	1.9
Error in M_s (%)	-	2.61	1.05	0.52

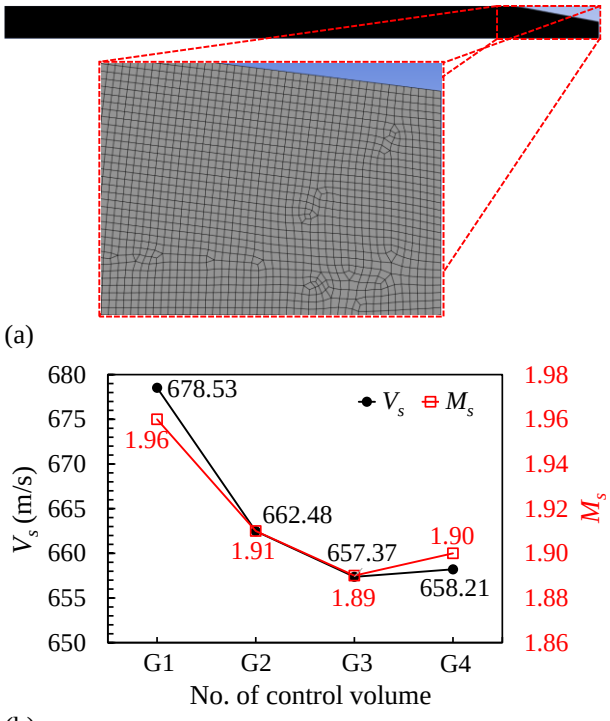

Fig. 4 (a) Discretized computational domain of the ST and (b) grid dependency test results

2.5 Grid Convergence Test

The investigation of grid independence is crucial in any numerical simulations to confirm that the results are not affected by the implemented discretization grid. The test is essential in ensuring the dependability and precision of numerical simulations. For this purpose, the simulation is conducted according to the different mesh sizes and time steps to reach the optimum combination of the mesh grid sizes.

2.5.1 CST domain

An orthogonal unstructured grid is adopted to discretize the computational domain of the ST (Fig. 4a). The time step size value of $7\text{x}10^{-8}$ and a Courant number of 0.25 are taken for the stability of the solver. For the study of grid dependency, four distinct grid sizes are used, each associated with specific control volume (CV) and shock velocities, as shown in Table 1. The respective M_s and error analyses are also formulated in Table 1. Initially, a grid size of 1 mm is used for the mesh generation. Later, the mesh sizes are refined to 0.5 mm, 0.1 mm, and 0.05 mm to obtain the optimal condition. Figure 4b depicts that

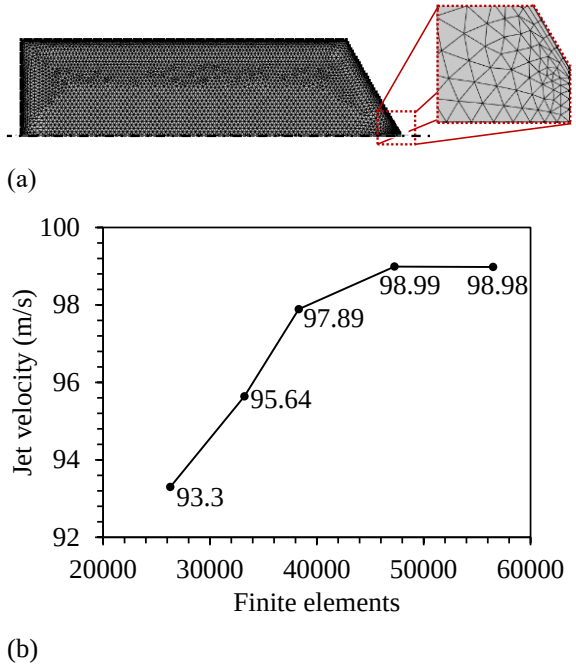

Fig. 5 (a) Discretized model of the DNC and (b) effects of grid sizes on the jet velocity

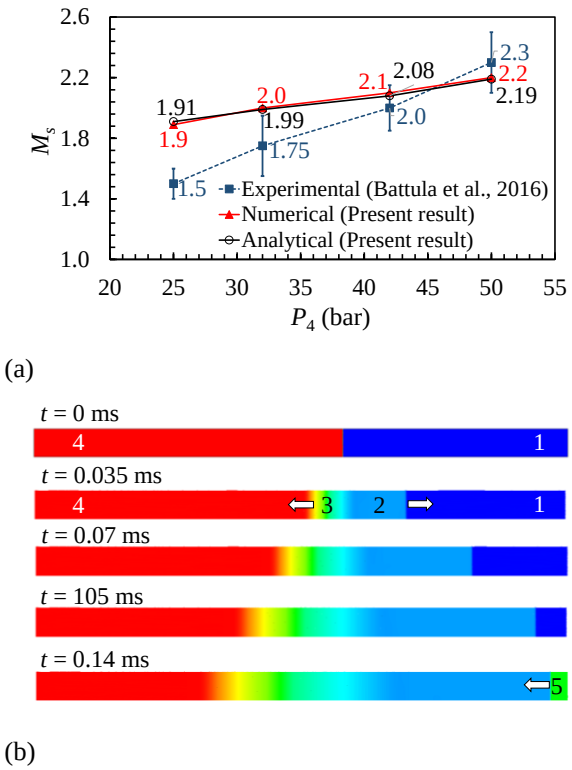

Fig. 6 (a) Comparison of numerical results with analytical and experimental and (b) shock pressure distribution inside PST at various time

an increase in CVs leads to the convergence of the V_s and the M_s. It is observed that the grid size of 0.1 mm (G3) having CVs of 368874 gives the minimum deviation in V_s and M_s with 0.77% and 1.05%, respectively. The additional modification in the grid did not result in any changes in the computation results. Therefore, it is appropriate to consider 0.1 mm as an independent grid size with appropriate flow field resolution for all remaining simulations, including validation.

2.5.2 DNC domain

A triangular unstructured mesh is used to discretize the fluid domain of DNC (Fig. 5a) to study the effects of grid sizes on the flow velocity of the jet. For the grid convergence study, consideration is given to a finite element of 26290, 33226, 38313, 47271, and 56504. The effects of grid values on the specific V_{jet} are depicted in Fig. 5b. The adopted grid of total element 47271 is given a jet velocity of 98.99 m/s, which established a minimal error in V_{jet} of 1.11%. Consequently, the computational domain is discretized utilizing a finite element of 47271 in all investigations, including validation.

2.6 Model Validation

Equations (12-16) are used to validate the present numerical results analytically for the ST simulation. Previously published experimental work is also used to validate the present solver, scheme, and model. The experimental data is collected from the work reported by Battula et al. (2016), where a 170 mm long and 20 mm diameter of PST was studied at a diaphragm pressure ratio of 25-50. The pressure of the driven region was maintained at 1 bar, whereas the pressure of the driver section was set to 25-50 bar for the initializations. The shock velocity and shock Mach numbers obtained from the present numerical simulations agree well with the analytical results attained from the ideal shock tube theory. It is observed that the maximum error in M_s deviates from the analytical result by less than 1%. But a deviation of 15.7%, 2.5%, 2.4% and 13.6 % in M_s at 25, 32, 42, and 50 bar (P_4), respectively, from experimental results, are obtained (Fig. 6a). The study indicates that there are minor differences between the observed and acceptable deviations for the numerical and analytical results. However, the impact of the shock wave on the real gas caused high viscous effects, and the heat transfer between the tube walls and shock-heated gas led to more significant attenuation in the experimental study. Therefore, it is feasible to draw the conclusion that the numerical technique utilized in this investigation is capable of accurately predicting flow parameters in the ST by a reasonable margin.

To provide a clear understanding of the shock dynamics within the ST, Fig. 6b vividly illustrates the pressure contours to visualize the propagation of shock waves over time. At t = 0 indicates the initial shock wave setup, with a sharp pressure difference between the high-pressure region (labelled as 4) and the low-pressure region (labelled as 1). Following the instant rupture of the diaphragm, the shock wave travels downstream of the tube at supersonic speeds (t = 0.035-0.105 ms). Simultaneously, an expansion fan moves towards the left-hand side, causing a pressure drop in the high-pressure region. Throughout the process, a distinct region (labelled as 2) is formed behind the incident shock, and another region (labelled as 3) is generated behind the expansion wave. These two regions are separated by a contact surface (Rathakrishnan, 2020). Across the shock front, there is an abrupt increase in pressure, temperature, and density. This

Table 2 Comparison of numerical results with analytical and experimental data

Results	V_{jet} (m/s)	% error
Numerical result	67.01	-
Analytical result	66.38	0.93
Experimental result (Battula et al., 2016)	65.12	2.8

occurs because the medium ahead of the shock wave is compressed into a higher state. Furthermore, the shock continues to move downstream and starts reflecting after reaching the end wall of the ST (t = 0.14 ms). Considering the findings and the propagation of shock waves within the ST, it is justifiable to conclude that the numerical method utilized in this study can accurately predict flow characteristics in micro-ST with a reasonable level of accuracy.

Additionally, the work also entails validating a numerical simulation driven by Eq. (6-11) by a comparison of its results with experimental data from Battula et al. (2016). The present simulation results are also compared with the empirical relation $V_{jet} = \sqrt{2 \times P_5 / \rho_i}$ derived from Bernoulli's equation (Battula et al., 2016). The experimental setup involved a circular tube with a diameter of 20 mm and a micronozzle diameter of 0.125 mm. The total length of the drug cavity is 20 mm, and a rubber membrane of 0.2 mm thickness isolates it from the PST. The rubber membrane exhibits 20±2 bar shock pressure during the operation. According to the experiment, the maximum microjet velocity was 65.12 m/s (Battula et al., 2016). A simulation was conducted under the same conditions to validate the present numerical model and solver. The simulation results indicate a maximum microjet velocity of 67 m/s at the outlet of the nozzle, which shows a good agreement with the experimental data, having a small error margin of 2.8% (Table 2). The present numerical results also agree well with analytical calculations, having a 0.93% deviation. Therefore, it is concluded that the numerical method employed in this study predicts flow characteristics in the DNC with reasonable accuracy.

Additionally, Fig. 7 elucidates the velocity distribution of a microjet within a DNC. The primary illustration depicts the velocity field with an enlarged segment concentrating on the outlet region where velocity gradients are most pronounced. The contour reveals a substantial increase in flow velocity near the outlet. The highest velocity attains around 67 m/s at the tip of the nozzle outlet. The elevated velocity is due to the converging nature of the nozzle design, which accelerates the flow as it passes through the narrower part.

3. RESULTS AND DISCUSSIONS

Following the successful completion of the validation process, simulations are performed to assess the behaviour of shock within the CST with regard to the fluctuation of flow characteristics of the shock wave. Initially, the

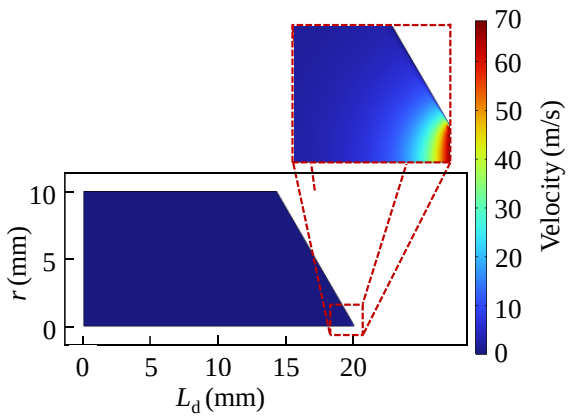

Fig. 7 Visualization of the microjet flow velocity

parametric study is carried out on a PST of the same geometry reported by Battula et al. (2016) to finalize the optimal dimension of L_c and r_c. The study aims to attain a better understanding of the wave dynamic focusing phenomenon near the converging zone. It assists in understanding the behaviour of the shock wave through converging channels, enhancing peak pressures, and achieving specific flow characteristics of the shock wave.

3.1 Analysis of CST

A fluid domain of the CST is used to conduct a parametric simulation, which allows an in-depth investigation of the wave dynamics due to the converging channels. For this purpose, geometrical modifications are performed on PST, considering a converging channel length L_c and end wall radius of the tube r_c to acquire a higher value of P_5. The total length (L_s) of the CST is considered to be 170 mm for the present simulation.

3.1.1 Effects of L_c

A comprehensive analysis has been conducted on the flow dynamics of the shock wave, which are influenced by geometric modifications to the PST. The main focus is to finalize the dimensions of the converging channel by explicitly adjusting the length L_c (20 mm with corresponding angle θ = 14.03º, 40 mm, θ = 7.12º, and 60 mm, θ = 4.76º) from the end wall of the ST, whereas the value of r_c is taken as 5 mm initially. The geometry of CST (Fig. 2a) clearly depicts that as the value of L_c increases, the angle θ decreases while keeping r_c constant. To maintain consistency in the analysis, this section employs N_2 at (P_4) 25 bar and air at (P_1) 1 bar in the driver and driven sections, respectively. Both fluids are initially sustained under isothermal conditions at $T_4 = T_1$ = 298 K.

Figure 8a depicts the temporal pressure distribution associated with different values of L_c with the comparison of PST. In the case of the PST, the peak reflected pressure (P_5) is measured as 23.4 bar. However, by incorporating a converging channel, the reflected pressure experienced a substantial rise to 26.3, 31.4, and 37.7 bar for 20, 40, and 60 mm of L_c, respectively, while keeping the operational pressure constant (Fig. 8a). The study revealed that a constant pressure region occurs before the shock enters the converging channel, resulting in a stabilized flow.

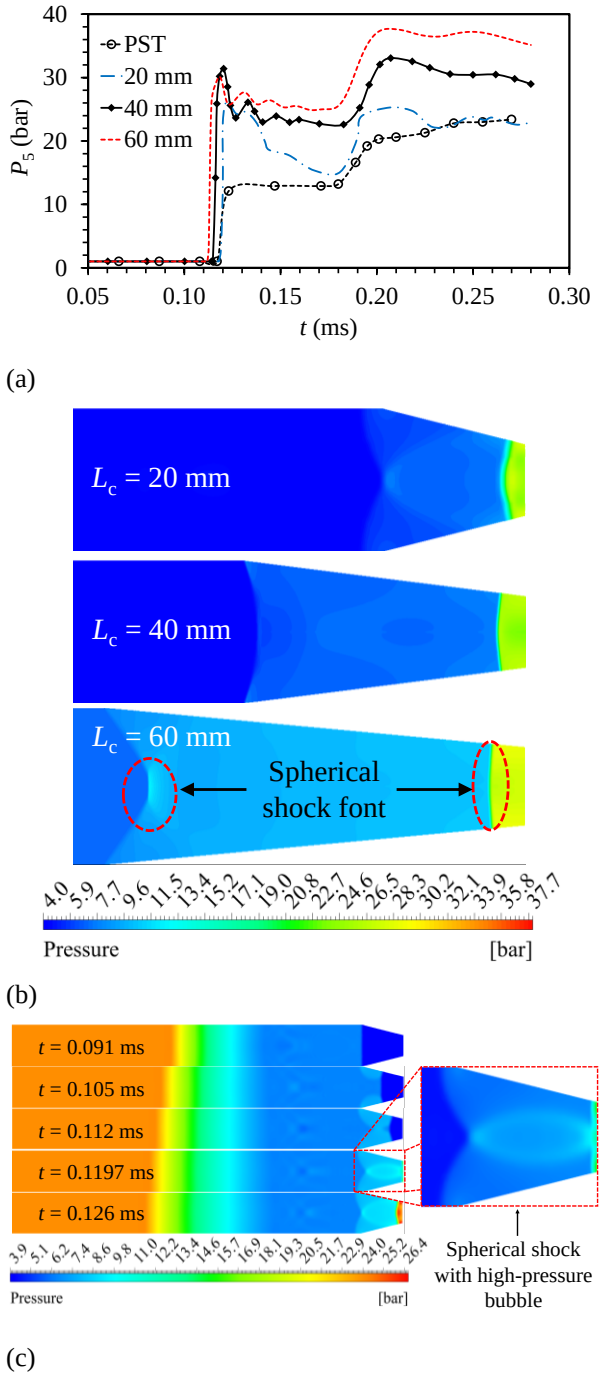

Fig. 8 (a) Temporal pressure variation (b) pressure distribution inside CST with various L_c and (c) shperical shock font inside the CST at different t

Furthermore, when the shock enters the converging zone, a sharp increase in the pressure is observed due to the sudden change in the cross-sectional area. However, the pressure spike post-shock is severe for all profiles. The timing of this rise is slightly affected by the channel length, resulting in larger channels exhibiting the highest pressure. Therefore, the study is evident that the shortest channel (L_c = 20 mm) exhibits the lowest peak pressure and more pronounced oscillations due to a rapid reflection of the shock wave and less controlled compression. Moreover, the most consistent and elevated pressure response is generated by the maximum extended converging channel ((L_c = 60 mm).

The contours depicted in Fig. 8b showcase the effect of different converging channel lengths (L_c) and corresponding angles (θ) on the pressure distribution within the CST. In the scenario of L_c = 20 mm with θ =14.03^o, the pressure distribution exhibits a notable growth as the fluid moves through the converging region. From the other side, the rarefaction of the reflected wave further compresses the fluid, leading to a rise in the pressure near the outlet of the converging section. However, due to the short duration, the pressure magnitude at the exit is very mild and localized. These findings indicate that the sharp convergence angle leads to inadequate time and space for pressure accumulation, limiting the homogeneity of the shock profile. Furthermore, increasing the L_c (40 mm and 60 mm) and decreasing the angles (θ = 7.12^o and 4.76^o) facilitate a more gradual convergence. This arrangement provides more space for the shock wave to compress the fluid within the converging portion, leading to a higher pressure magnitude near the outlet. Therefore, the longest L_c (60 mm) and smallest θ (4.76^o) ensures the most efficient shock convergence with the highest pressure intensification. Therefore, the observed rise of approx. 61% in reflected pressure serves to underscore the efficacy of the geometric change in comparison with PST. Hence, the length of 60 mm is determined to be the most favourable dimension for all upcoming studies, ensuring the best performance in terms of pressure enhancement within the CST.

The contours (Fig. 8b) also depict the formation of a spherical shock font, which is inadequate for the precise application of drug delivery. To study the complex flow dynamics of a shock wave within a CST, the pressure distribution at different time intervals ranging from t = 0.091 ms to 0.126 ms are depicted in Fig. 8c. The contour plots provide an intense visualization of the high-pressure regions developing near the end wall of the ST. As the shock wave progresses, a significant observation is made at t = 0.105 ms, where the shock wave enters the converging zone. At this point, shock reflections begin to manifest as bubbles along the converging edges. These shock reflection bubbles gradually grow in size as time advances to t = 0.112 ms. A particularly fascinating phenomenon occurs at t = 0.1197 ms when the shocks from both converging edges collide, resulting in the formation of a high-pressure bubble. This collision alters the behaviour of the shock wave, transforming it into a spherical shock. At time t = 0.126 ms, the spherical shock wave proceeds downstream through the converging channel and finally strikes the end wall of the ST. A zone of exceptionally high pressure is formed at the end wall as a result of this collision.

Nevertheless, it is essential to acknowledge that the pressure distribution throughout the end wall is not uniform, therefore presenting a drawback for drug delivery applications that need constant and regulated pressure. In order to tackle this problem, additional criteria are considered to alter the shock wave characteristics. Considerations are given to incorporate a flat segment of length L_f in CST (CSTF) to convert the spherical shock into a normal shock. The study is presented in the upcoming section.

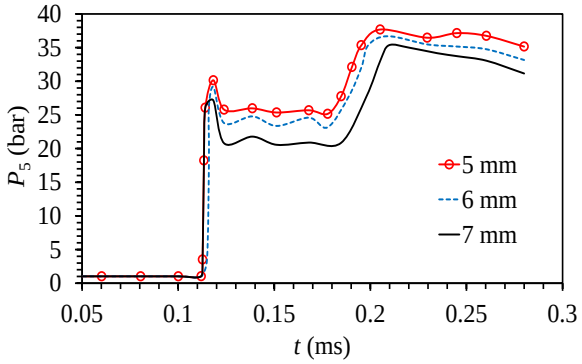

Fig. 9 Temporal pressure distribution at 60 mm of L_c and different r_c

3.1.2 Effects of r_c

An extensive parametric analysis is performed in this section to ascertain the optimal end wall radius of the CST by adjusting the radius (r_c) values from 5mm, 6mm, and 7mm, whereas the L_c is constant. Figure 9 depicts the temporal pressure profiles obtained at varying r_c of the CST. The research shows that when the radius of the end wall (r_c) for the converging channel grows from 5 mm to 7 mm, the maximum peak pressure decreases slightly but considerably from 37.7 bar to 31.15 bar. These findings suggest that the radius of the end wall is a critical factor in determining the reflected pressure within the CST. The correlation between the radius of the end wall and the pressure profile implies that precise adjustment of r_c is crucial for maximizing the efficiency of the CST, especially in attaining the intended pressure settings for the specified operation.

The most appropriate shape for the converging channel has been determined based on the trends (Fig. 9). The optimal design parameters consist of a channel length L_c of 60 mm with θ = 4.76° and an end wall radius r_c of 5 mm. Care has been taken to finalize the optimal parameters as it offers a compromise between maximizing peak pressure and ensuring the intended pressure distributions.

3.2 Analysis of CSTF

Following the behaviour of shock dynamics in the CST, a flat segment of length L_f is attached after the L_c to change the spherical shock behaviour to normal shock. The changes are made to attain the goal of a more homogeneous distribution of pressure across the end wall boundary. It is crucial to make this modification in order to optimize the ST design for medication delivery. A comprehensive analysis is performed to finalize L_f in the shape of the CSTF. Therefore, the final design that includes the converging channel with the recently introduced flat portion of CSTF is represented in Fig. 10. This technique ensures that the shock wave characteristics conform to the exact criteria for efficient and dependable therapeutic administration.

3.2.1 Effect of L_f

The provided pressure-time curve (Fig. 11) depicts the temporal variation of reflected shock pressure (P_5) at

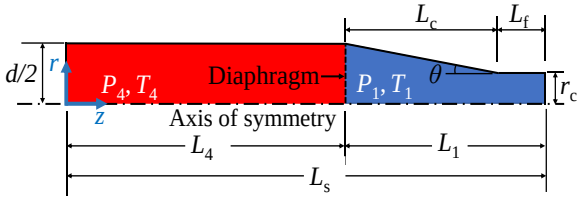

Fig. 10 Geometry of the CSTF

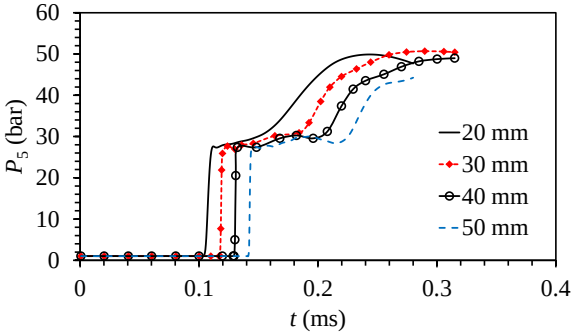

Fig. 11 Temporal pressure distribution at different L_f and

different axial distances (L_f = 20, 30, 40, 50 mm) within a shock tube scenario. Each curve illustrates the transmission and effect of the shock wave, providing insights into the shock dynamics at different lengths of the flat segment in the CSTF shape. It is observed that the initial pressure remains low and steady (t < 0.1 ms) at all distances. It signifies that the fluid is undisturbed prior to the shock wave's arrival. With the passage of time, at approx. t = 0.1 ms, a sharp jump in pressure across all four curves is observed. The sudden rise indicates the instantaneous energy transfer and the significant compression of the fluid produced by the reflection as the shock wave hits the end wall. After the initial surge, the pressure stabilizes with a distinct value based on the length of the L_f. For 20 mm and 30 mm lengths of L_f, the pressure reaches its peak rapidly and stabilizes at around 50 bar. It demonstrates the most intense impact due to the proximity to the shock source, whereas at L_f = 30 mm, the pressure rise is slightly delayed but more gradual stabilization. It also exhibits minor fluctuations in pressure immediately following the initial rise. The observed oscillations suggest the presence of instability in the reflection of the shock wave due to the interaction of the shock with the converging geometry. For L_f = 40 mm and L_f =50 mm, the peaks become increasingly delayed and less pronounced, illustrating the shock's energy dissipating as it travels further downstream.

Based on the parametric study, the flat segment length is finalized as 30 mm, followed by L_c = 60 mm with θ = 4.76° and r_c = 5 mm. This specific configuration of the CSTF (L_s = 200 mm) demonstrated superior performance when compared to CST and PST. The extended flat segment length of 30 mm not only enhances the overall performance but also facilitates practical considerations. It provides sufficient space for integrating pressure and temperature probes, paving the way for experimental

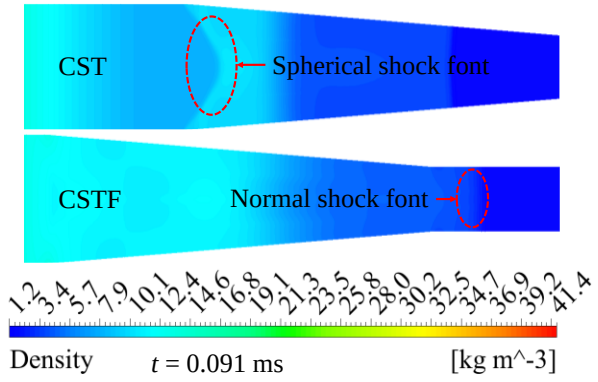

(a)

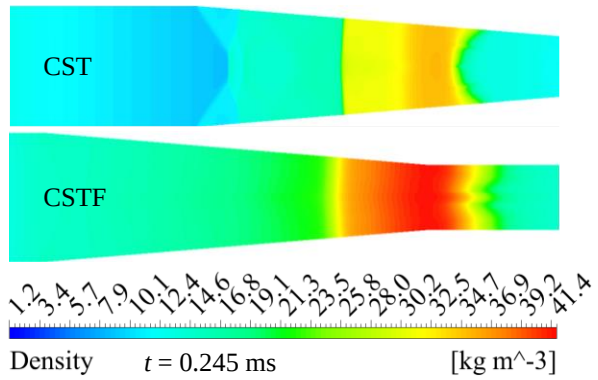

(b)

Fig. 12 Comparison of density distributions at (a) t = 0.091 ms and (b) t = 0.245 ms between CST and CSTF

advancements and real-time monitoring in future studies. This thoughtful design ensures both functional efficiency and adaptability for experimental setups, making CSTF the preferred configuration.

3.3 CSTF vs. CST

In the previous section, the geometrical parameters of the CST that influence the pressure distribution within the ST have been explored. The focus was on enhancing the reflected shock pressure P_5 with uniform distribution across the boundary. The study on the CST showed an increase in P_5, but it also resulted in a spherical shock font with non-uniform pressure distribution across the end wall (Fig. 8). Therefore, this section aims to achieve a uniform distribution of pressure across the wall boundary while maintaining the strength of P_5. The density distributions shown in Fig. 12a and Fig. 12b represent the contours before reflection (t = 0.091 ms) and after reflection of the shock (t = 0.245 ms). It illustrates the dynamic behaviour of the shock wave as it traverses the channel. This figure exemplifies the comparison of density distribution within the CST and CSTF. For ease of depiction, the shock waves focusing zone in the driven region is highlighted in the contour's representation. The configuration has specific geometric and flow characteristics, influencing the shock propagation and density variations.

At t = 0.091 ms, the contour exhibits a very consistent and low-density gradient along the converging zone (Fig. 12a). At this preliminary phase, the shock wave has not yet produced much compression, and the density remains uniform. The setup phase is crucial, as it facilitates the initial accumulation of the shock wave's energy in preparation for its intensification and downstream propagation. Furthermore, at t = 0.245 ms, a remarkable transformation has emerged (Fig. 12b). As the shock wave travels, the narrowing cross-section compresses the flow, leading to a rise in the density downstream. The CSTF configuration demonstrates a smooth density contour, signifying steady shock propagation without substantial wave disruptions compared to CST. Moreover, a significant density appeared near the exit of the converging zone. The focusing effect amplifies shock pressure, steering to pronounced gradients and high-density regions compared to CST.

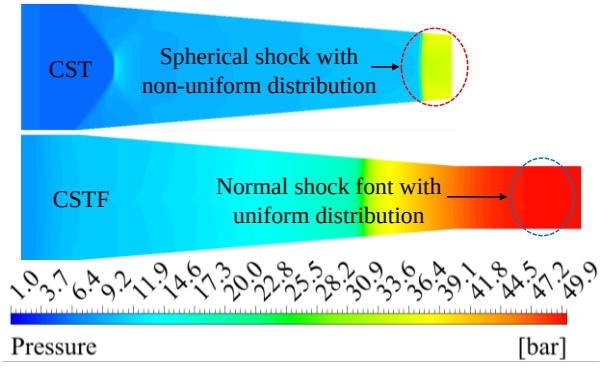

Fig. 13 Uniformly distributed high-pressure region at the best suitable design of CSTF

In addition, the behaviour of spherical shock inside the CST is changed to normal shock when it enters the flat segment in CSTF. In this case, the density distribution exhibits a comparatively high concentration near the inlet of a flat segment (Fig. 12b), which subsequently reduces as it progresses through the flat segment. It resulted in a gradual transition in density with more uniform distributions.

Figure 13 illustrates the comparison of pressure distribution at an optimal dimension of the CSTF with CST. The contour illustrates a spherical shock front and an irregular pressure distribution throughout the cross-section at the exit in CST. The shock wave demonstrates increased pressure intensity along the centre axis, whereas the periphery areas encounter reduced pressure. This irregularity results in ineffective energy transfer and variable performance in downstream applications. In addition, the diagram effectively shows the transformation of the shock wave from a spherical font to a normal font as it travels through the flat region of the CSTF. The shock wave initially propagates in all directions, forming a spherical font. Nevertheless, as it advances and comes into contact with the flat segment of the tube, the shock front gradually becomes more focused and consistent, finally creating a homogeneous pressure distribution. The procedure not only substantially raises the pressure but also aligns the shock front to establish a homogeneity in distribution, which is optimal for delivering the maximal force in a highly regulated way. Moreover, the modification is essential for the implementation of NDDS,

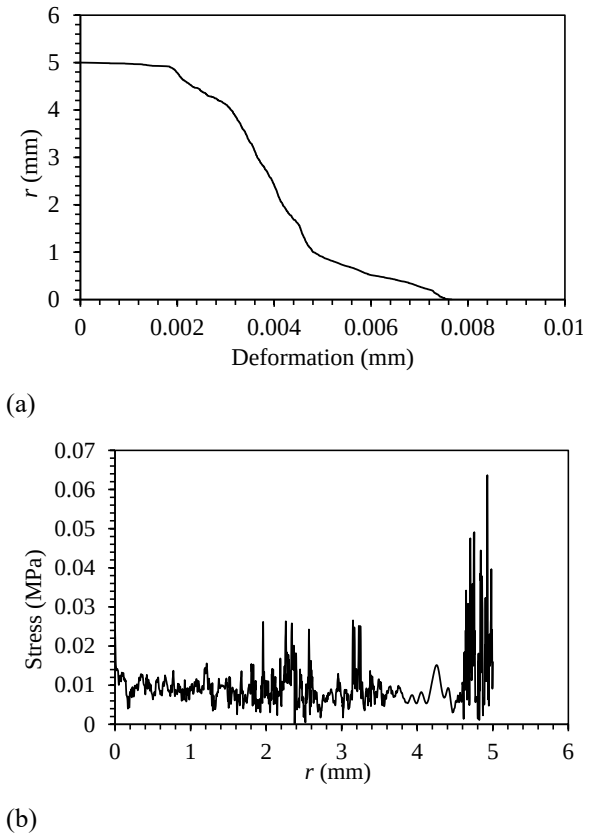

Fig. 14 Distribution of (a) deformation and (b) stress across the radius of the membrane

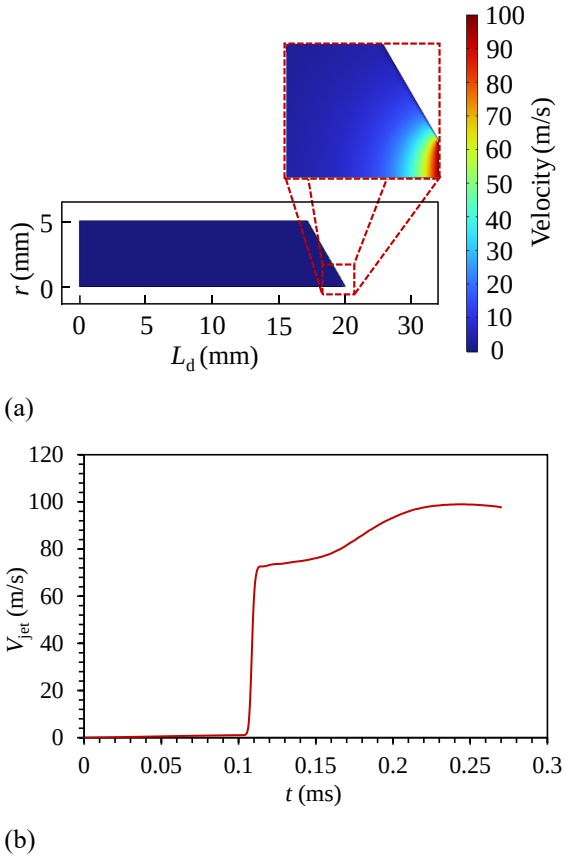

Fig. 15 (a) Distribution of maximum jet velocity at the outlet of the nozzle and (b) temporal variation of the jet velocity

which requires consistent and regulated pressures to ensure precise and efficient delivery of the medicine. Hence, the CSTF design surpasses the CST by generating a uniform and normal shock font with improved pressure consistency.

3.4 DNC with CSTF

The DNC is integrated with CSTF through a HEM to facilitate the execution of drug delivery. The DNC serves as a container for the drug. The high-pressure intensity of the shock wave induces an elastic deformation in the HEM. Consequently, the liquid drug is expelled through the nozzle as a high-velocity (V_{jet}) microjet. The deformation dynamics of the HEM and jet velocity are discussed next.

3.4.1 Deformation Dynamics of the HEM

Following the FSI simulation, Fig. 14a shows the temporal variation in deformation on the membrane after the shock wave loading. The shock initially hits the membrane, causing it to deform as it absorbs the shock energy. The deforming membrane executes the ejection of the drug in the form of a jet. It is observed that the maximum deformation of 0.007 mm appeared at the centre of the membrane. This suggests that the maximum deformation is taking place near the central region due to stress concentration or load at the centre. Furthermore, the reduction in the rate of deformation near the edges (at r_c = 5 mm) becomes steeper, which indicates a more rapid drop in the deformation. This is due to boundary constraints and material properties changing significantly at this point. In such cases, clamping or support conditions cause the structure to resist further deformation more effectively.

Figure 14b depicts the variation of stress along the radial distance of the HEM under the shock loading condition. The maximum stress appeared near the boundary edges of HEM (at r_c = 5 mm). This can be attributed to the clamped boundary condition that restricts displacement and intensifies stress concentration. The stresses are relatively low but fluctuate subtly towards the centre of the HEM. These variations arise from the material's inherent elastic properties, which help dissipate the applied shock energy more evenly in this region. The maximum stress observed is 0.063 MPa, which is under the yield stress limit of the material. It confirms the structural integrity of the HEM during the ejection of the liquid drug. This investigation highlights the capacity of the material to withstand high-stress conditions while preserving its elasticity and preventing failure.

3.4.2 Jet Velocity of the Liquid Drug

Figure 15a illustrates the velocity contour of a jet flow influenced by the shock wave pressure. The contour effectively describes the velocity distribution inside the DNC, highlighting the dynamics of the flow. It is observed that the maximum flow velocity of the jet is focused at the tip of the outlet. It denotes the area where the energy of the shock wave is most efficiently transmitted to the jet flow. The progressive rise in velocity throughout the channel signifies the acceleration effect produced by the design of

the nozzle. The amplification of velocity is an important factor for optimizing the jet performance and understanding the flow dynamics of jet under the shock-driven scenario.

Figure 15b depicts the temporal distribution of the jet velocity at the centre point of the outlet. The observed maximum jet velocity is 98.9 m/s, which is attained around t = 0.245 ms. The graph shows a characteristic behaviour of the jet, where the fluid is initially accelerated, and then it reaches the steady state condition. This nature indicates an effective energy transfer from the shock wave to the jet, with fast initial acceleration resulting directly from the shock-induced pressure gradient. The steady-state phase signifies the balance of forces influencing the fluid, ensuring uniform jet flow post-shock interaction. Hence, the achieved jet velocity is sufficient to propel the liquid drug inside the subcutaneous layer of the skin (Portaro et al., 2019).

4. CONCLUSIONS

A novel CSTF is proposed to enhance the performance and reflected pressure for NDDS. A detailed parametric analysis was performed to finalize the design by considering various geometric modifications to achieve the desired outcomes. Furthermore, FSI analysis has been performed to ensure the reliability of the system under operational conditions, particularly in precise applications of drug delivery systems. Following the comprehensive analysis, the below outcomes may be derived.

- A parametric analysis of the CST, achieved by altering the converging channel length L_c and radius r_c demonstrates an increase in the reflected pressure P_5. However, it is important to note that the pressure distribution at the end wall boundary is not uniform, leading to the formation of a spherical shock wave. Such unpredictability is a problem for medication delivery systems that need consistent and regulated pressure to achieve the best effectiveness.
- To tackle the problem of spherical shock font, a flat segment of 30 mm (L_f) after the converging region is finalized after the comprehensive analyses.
- The study emphasizes the significance of achieving convergence in channel length as a means to enhance the efficiency of the ST. With an increase in L_c, the peak pressure also increases, leading to an enhancement in overall pressure stability.
- The effect of L_c and angle θ on the distribution of density inside the ST is examined. As the value of L_c increases, θ decreases, which leads to a smoother and uniform density transition. The gradual rise in density is helpful for enhancing shock wave dynamics, as it allows a smoother and more regulated energy transfer within the ST.
- From the parametric analysis, the CSTF having 60 mm of L_c with θ = 4.76°, 5 mm of r_c and L_f = 30 mm have superior performance with approx. 113.2% higher P_5 (49.9 bar) compared to PST and 32.3% compared to CST.
- These modifications provided a normal shock with a homogenous transition of pressure across the wall boundary, which is essential for NDDS.
- The maximum deformation is observed at 0.007 mm near the centre of the HEM. This study examines the radial deformation of a structure under load, highlighting that maximum deformation occurs at the centre and decreases towards the boundary.
- The peak stress induced on HEM during the FSI simulation is 0.063 MPa. The stress distribution revealed the highest values near the clamped boundary of the membrane, while the lowest stresses were concentrated around the centre of the membrane.
- The maximum jet velocity at the tip of the outlet is observed at 98.9 m/s, which indicates a significant achievement for injecting the drug into the soft target.

Therefore, the proposed model of the CSTF is the better choice for generating more pressure at minimum working pressures. For the brevity of the work, limited geometric parameters have been adopted in this study. One can adopt more parameters to obtain the desired output. This specific measurement is essential for evaluating the structural integrity and potential failure modes of the solid membrane under stress. Moreover, the different material properties of the solid membrane yields the drug ejection characteristic, viz., jet cone angle, jet diameter, and the impinging pressure on the target surface, etc. Therefore, effects on various jet characteristics and failure criterion analysis of solid membrane might be helpful for further study to optimize the system.

ACKNOWLEDGEMENTS

The authors would like to thank the Department of Mechanical Engineering, National Institute of Technology Meghalaya, for providing the necessary resources. The authors are also grateful to Mr. Pratit Sundar Dev Roy for his unwavering cooperation in running the program efficiently.

CONFLICTS OF INTERESTS

The authors have not received funding from any agencies and declare no conflict of interest.

AUTHORS CONTRIBUTION

Zeyaullah Ansari: Conceptualization, Formal analysis, Investigation, Methodology, Software, Validation, Visualization, Writing-original draft, Writing-review & editing. **Koushik Das:** Conceptualization, Data curation, Investigation, Methodology, Project administration, Software, Supervision, Visualization, Writing-review & editing. **Ramesh Babu Pallekonda:** Project administration, Supervision, Visualization.

REFERENCES

Ali, M. A., & Mondal, P. (2025). Numerical investigation of impinging planar shock wave interaction with axisymmetric slender body. *Journal of Applied Fluid Mechanics*, *18*(3), 809-820. https://doi.org/10.47176/jafm.18.3.2768.

Amir, A. F., Yusoff, M. Z., & Yusaf, T (2008). Numerical Simulation of inviscid transient flows in shock tube and its validations. *International Journal of Physical and Mathematical Sciences*, *2*(7), 409-419. https://doi.org/10.5281/zenodo.1331555.

Battula, N., Menezes, V., & Hosseini, H. (2016). A miniature shock wave driven micro-jet injector for needle-free vaccine/drug delivery. *Biotechnology and Bioengineering*, *113*(11), 7. https://doi.org/10.1002/bit.26016

Bayazidi, S., Mojaddam, M., & Mohseni, A. (2023). Performance optimization of nozzle-diffuser piezoelectric micropump with multiple vibrating membranes by design of experiment (DOE) method. *Journal of Applied Fluid Mechanics*, *16*(7), 1356-1370. https://doi.org/10.47176/jafm.16.07.1539.

Boulahia, A., Abboudi, S., & Belkhiri, M. (2014). Simulation of viscous and reactive hypersonic flows behaviour in a shock tube facility: TVD schemes and flux limiters application. *Journal of Applied Fluid Mechanics*, 7(2), 315-328. https://doi.org/10.36884/jafm.7.02.19390.

Debnath, S., Saha, A. K., Siddheshwar, P. G., & Roy, A. K. (2019). On dispersion of a reactive solute in a pulsatile flow of a two-fluid model. *Journal of Applied Fluid Mechanics*, *12*(3), 987-1000. https://doi.org/10.29252/jafm.12.03.29101

Hankare, P., Agrawala, A., & Menezes, V. (2022). High-Speed Jet Injector for Pharmaceutical Applications. *Journal of Medical Devices*, *16*(3), 034502. https://doi.org/10.1115/1.4054549

Henshall, B. D. (1957). Some aspects of the use of shock tubes in aerodynamic research. *Aeronautical Research Council Reports and Memoranda*, *3044*.

Houser, T. A., Sebranek, J. G., Baas, T. J., Thacker, B. J., Nilubol, D., & Thacker, E. L. (2003). Feasibility of transdermal, needleless injections for prevention of pork carcass defects. *Iowa State University Animal Industry Report*, *1*(1), 1. https://doi.org/10.1016/j.meatsci.2004.03.016.

Jagadeesh, G., Prakash, G. D., Rakesh, S. G., Allam, U. S., Krishna, M. G., Eswarappa, S. M., & Chakravortty, D. (2011). Needleless vaccine delivery using micro-shock waves. *Clinical and Vaccine Immunology*, *18*(4), 539-545. https://doi.org/10.1128/CVI.00494-10

Kanwar, S. S., Dubey, G., Singh, M., & Khanday, G. S. (2015). CFD Analysis of normal shock using shock tube with five species. *International Journal of Science and Research*, *4*(8), 1900-1905. https://doi.org/10.21275/25081501.

Kazi, A., Kakde, A. P., Khaire, M. P., & Chhajed, P. N. (2018). Needle free injection device: The painless technology. *MIT International Journal of Pharmaceutical Sciences*, *4*(2), 6.

Kendall, M. A. F. (2002). The delivery of particulate vaccines and drugs to human skin with a practical, hand-held shock tube-based system. *Shock Waves*, *12*(1), 23-30. https://doi.org/10.1007/s001930200126

Kim, B., Lee, S. B., Lee, J., Cho, S., Park, H., Yeom, S., & Park, S. H. (2012). A comparison among Neo-Hookean model, Mooney-Rivlin model, and Ogden model for chloroprene rubber. *International Journal of Precision Engineering and Manufacturing*, *13*(5), 759-764. https://doi.org/10.1007/s12541-012-0099-y

Kiyama, A., Endo, N., Kawamoto, S., Katsuta, C., Oida, K., Tanaka, A., & Tagawa, Y. (2019). Visualization of penetration of a high-speed focused microjet into gel and animal skin. *Journal of Visualization*, *22*(3), 449-457. https://doi.org/10.1007/s12650-019-00547-8

Kjellander, M., Tillmark, N., & Apazidis, N. (2010). Shock dynamics of strong imploding cylindrical and spherical shock waves with real gas effects. *Physics of Fluids*, *22*(11), 116102. https://doi.org/10.1063/1.3500684

Lewin, S., & Skews, B. (2020). Propagation of shock waves of varying curvature. *Journal of Applied Fluid Mechanics*, *14*(3), 691-701. https://doi.org/10.47176/jafm.14.03.31956.

Liu, Y., & Kendall, M. A. F. (2007). Optimization of a jet-propelled particle injection system for the uniform transdermal delivery of drug/vaccine. *Biotechnology and Bioengineering*, *97*(5), 1300-1308. https://doi.org/10.1002/bit.21324

Menezes, V., Kumar, S., & Takayama, K. (2009). Shock wave driven liquid microjets for drug delivery. *Journal of Applied Physics*, *106*(8), 086102. https://doi.org/10.1063/1.3245320

Mukhambetiyar, A., Nazarbayev University, Jaeger, M., University of Tasmania, Adair, D., & Nazarbayev University. (2017). CFD modelling of flow characteristics in micro shock tubes. *Journal of Applied Fluid Mechanics*, *10*(4), 1061–1070. https://doi.org/10.18869/acadpub.jafm.73.241.27474.

Muritala, A. O., Skews, B. W., & Craig, L. (2015). A study of the complex flow features behind a diffracted shock wave on a convex curved wall. *Journal of Applied Fluid Mechanics*, *8*(4), 667-672. https://doi.org/10.18869/acadpub.jafm.67.223.20428.

Nakayama, H., Portaro, R., Kiyanda, C. B., & Ng, H. D. (2016). CFD modeling of high speed liquid jets from an air-powered needle-free injection system. *Journal of Mechanics in Medicine and Biology*, *16*(04),

1650045. https://doi.org/10.1142/S0219519416500457

Nanda, S. R., Agarwal, S., Kulkarni, V., & Sahoo, N. (2017). Shock Tube as an impulsive application device. *International Journal of Aerospace Engineering*, *2017*, 1–12. https://doi.org/10.1155/2017/2010476

Park, J. H., Allen, M. G., & Prausnitz, M. R. (2006). Polymer microneedles for controlled-release drug delivery. *Pharmaceutical Research*, *23*, 1008-1019. https://doi.org/10.1007/s11095-006-0028-9

Portaro, R., Sadek, J., Xu, H., & Ng, H. D. (2019). Controlled release using gas detonation in needle-free liquid jet injections for drug delivery. *Applied Sciences*, *9*(13), 2712. https://doi.org/10.3390/app9132712

Rakesh, S. G., Gnanadhas, D. P., Allam, U. S., Nataraja, K. N., Barhai, P. K., Jagadeesh, G., & Chakravortty, D. (2012). Development of micro-shock wave assisted dry particle and fluid jet delivery system. *Applied Microbiology and Biotechnology*, *96*(3), 647-662. https://doi.org/10.1007/s00253-012-4196-8

Rane, Y. S., & Marston, J. O. (2020). Computational study of fluid flow in tapered orifices for needle-free injectors. *Journal of Controlled Release*, *319*, 382-396. https://doi.org/10.1016/j.jconrel.2020.01.013

Rane, Y. S., & Marston, J. O. (2021). Transient modelling of impact driven needle-free injectors. *Computers in Biology and Medicine*, *135*, 104586. https://doi.org/10.1016/j.compbiomed.2021.104586

Rasel, M. A. I., & Kim, H. D. (2013). A numerical study of the gas and particle dynamics in a needle free drug delivery device. *Journal of Mechanical Science and Technology*, 27, 3103-3112. https://doi.org/10.1007/s12206-013-0829-9

Rathakrishnan, E. (2020). *Gas dynamics*. PHI Learning Pvt. Ltd.

Rathod, V., & Mahapatra, D. (2017). Optimization of a diaphragm for a micro-shock tube-based drug delivery method. *Bioengineering*, *4*(4), 24. https://doi.org/10.3390/bioengineering4010024

Schramm, J., & Mitragotri, S. (2002). Transdermal drug delivery by jet injectors: Energetics of jet formation and penetration. *Pharmaceutical Research*, *19*, 1673-1679. https://doi.org/10.1023/A:1020753329492.

Shankar, S. K., Kawai, S., & Lele, S. K. (2011). Two-dimensional viscous flow simulation of a shock accelerated heavy gas cylinder. *Physics of Fluids*, *23*(2). https://doi.org/10.1063/1.3553282.

Singh, G. P., Sharma, J. D., Arora, R., & Sandhu, I. S. (2020). CFD analysis of shock tube for blast impact testing. *Materials Today: Proceedings*, *28*, 1872-1878. https://doi.org/10.1016/j.matpr.2020.05.294.

Trimzi, M. A., & Ham, Y. B. (2021). A needle-free jet injection system for controlled release and repeated biopharmaceutical delivery. *Pharmaceutics*, *13*(11), 1770. https://doi.org/10.3390/pharmaceutics13111770.

Wang, L., & Kong, D. (2023). Study on pressure reconstruction method of explosion shock wave. *Journal of Applied Fluid Mechanics*, *16*(7), 1442-1454. https://doi.org/10.47176/jafm.16.07.1690.

Wang, Y., Yue, L., Hu, L., & Wang, J. (2021). Needle-free jet injectors' geometry design and drug diffusion process analysis. *Applied Bionics and Biomechanics*, *2021*(1), 5199278. https://doi.org/10.1155/2021/5199278

Wang, Z., Song, D., Wang, J., Xiong, L., Shi, T., Zhang, C., Di, L., Zhang, C., Zhang, Y., & Li, H. (2022). Simulation and experimental study on the influence of needle-free jet injection nozzle structure on injection performance. *Journal of Drug Delivery Science and Technology*, *68*, 103043. https://doi.org/10.1016/j.jddst.2021.103043.

Wijaya, U., Soegiarso, R., & Tavio. (2019). *Mechanical properties of Indonesian hyperelastic low-grade rubber for low-cost base isolator*. MATEC Web of Conferences, 276, 01017. https://doi.org/10.1051/matecconf/201927601017.

Yu, J., Zhang, X. P., Wang, J., Hao, Y., & Mao, H. B. (2025). Study on the shock wave characteristics of spherical and cylindrical explosives in near-field underwater explosion. *Journal of Applied Fluid Mechanics*, *18*(4), 892-903. https://doi.org/10.47176/jafm.18.4.2960.

Zhang, G., & Kim, H. D. (2015). Numerical simulation of shock wave and contact surface propagation in micro shock tubes. *Journal of Mechanical Science and Technology*, *29*(4), 1689-1696. https://doi.org/0.1007/s12206-015-0341-5

Zhang, G., Jin, Y.Z., Setoguchi, T. and Kim, H.D. (2016). Study on drug powder acceleration in a micro shock tube. *Journal of Mechanical Science and Technology*, *30*, 4007-4013. https://doi.org/10.1007/s12206-016-0813-2.

Zhang, G., Setoguchi, T., & Kim, H. D. (2015). Numerical simulation of flow characteristics in micro shock tubes. *Journal of Thermal Science*, *24*(3), 246-253. https://doi.org/10.1007/s11630-015-0780-4